Quantifying the Accuracy and Uncertainty of Diurnal Thermodynamic Profiles and Convection Indices Derived from the Atmospheric Emitted Radiance Interferometer

W. G. BLUMBERG

School of Meteorology, and Cooperative Institute for Mesoscale Meteorological Studies, University of Oklahoma, Norman, Oklahoma

T. J. WAGNER

Space Science and Engineering Center, and Cooperative Institute for Meteorological Satellite Studies, University of Wisconsin–Madison, Madison, Wisconsin

D. D. TURNER

NOAA/Earth System Research Laboratory, Boulder, Colorado

J. CORREIA, JR.

Cooperative Institute for Mesoscale Meteorological Studies, University of Oklahoma, and NOAA/Storm Prediction Center, Norman, Oklahoma

(Manuscript received 10 February 2017, in final form 1 June 2017)

ABSTRACT

While radiosondes have provided atmospheric scientists an accurate high-vertical-resolution profile of the troposphere for decades, they are unable to provide high-temporal-resolution observations without significant recurring expenses. Remote sensing technology, however, has the ability to monitor the evolution of the atmosphere in unprecedented detail. One particularly promising tool is the Atmospheric Emitted Radiance Interferometer (AERI), a passive ground-based infrared radiometer. Through a physical retrieval, the AERI can retrieve the vertical profile of temperature and humidity at a temporal resolution on the order of minutes. The synthesis of these two instruments may provide an improved diagnosis of the processes occurring in the atmosphere. This study provides a better understanding of the capabilities of the AERI in environments supportive of deep, moist convection. Using 3-hourly radiosonde launches and thermodynamic profiles retrieved from collocated AERIs, this study evaluates the accuracy of AERI-derived profiles over the diurnal cycle by analyzing AERI profiles in both the convective and stable boundary layers. Monte Carlo sampling is used to calculate the distribution of convection indices and compare the impact of measurement errors from each instrument platform on indices. This study indicates that the nonintegrated indices (e.g., lifted index) derived from AERI retrievals are more accurate than integrated indices (e.g., CAPE). While the AERI retrieval's vertical resolution can inhibit precise diagnoses of capping inversions, the high-temporal-resolution nature of the AERI profiles overall helps in detecting rapid temporal changes in stability.

1. Introduction

The radiosonde is widely considered to be the gold standard for measuring vertical profiles of thermodynamic and kinematic variables. The in situ nature of radiosonde observations allows scientists to obtain a high-vertical-resolution (roughly every 10 m) picture of the atmosphere. Because of this, radiosondes are used for several different applications. Meteorologists use these profiles to understand the current atmospheric state, initialize models, verify model forecasts, and infer physical processes that may yield convection. Although the measurements from radiosondes are valuable, they have a high marginal cost for each additional observation and are rarely used to create a high-temporal-resolution picture of the atmosphere.

Corresponding author: Greg Blumberg, wblumberg@ou.edu

DOI: 10.1175/JAMC-D-17-0036.1

By contrast, automated thermodynamic remote sensors, such as Atmospheric Emitted Radiance Interferometers (AERIs; Knuteson et al. 2004a,b), have a higher initial cost but smaller recurring costs for each additional observation. The AERI is a passive, ground-based hyperspectral infrared remote sensor from which high-temporal-resolution boundary layer thermodynamic profiles can be retrieved. Because of the passive nature of the AERI, its profiles have weaknesses that radiosondes do not possess. Primarily, the AERI spectra largely only describe the thermodynamic profile within the lowest 3 km of the atmosphere, and the retrieved profiles have a much lower vertical resolution than radiosondes (Turner and Löhnert 2014; Blumberg et al. 2015). Despite these issues, the high-temporal-resolution AERI profiles have demonstrated the ability to qualitatively identify destabilization trends in environments supportive of deep, moist convection when additional data about the mid- to upper troposphere are included in the AERI retrieval (e.g., Feltz and Mecikalski 2002; Feltz et al. 2003; Wagner et al. 2008).

Past studies have demonstrated the usefulness of other lower-vertical-resolution profiling instruments such as ground- and spaced-based multichannel microwave radiometers and infrared spectrometers (Feltz et al. 1998; Serio et al. 2008; Löhnert and Maier 2012; Di Natale et al. 2017). In particular, studies have analyzed how convection indices derived from these instruments can be used. For example, Koch et al. (2016) used ground-based multichannel microwave radiometer (MWR) retrievals to document and detect rapid changes in instability. Although multiple studies validating various MWR- and AIRS-derived convection indices against radiosondes have been published (e.g., Chan and Hon 2011; Madhulatha et al. 2013; Cimini et al. 2015; Pushpa Saroja et al. 2016; Gartzke et al. 2017), no study of this type exists in the scientific literature for the AERI. Currently, the literature only documents brief evaluations of AERI-derived convection indices (e.g., Feltz and Mecikalski 2002; Feltz et al. 2003). In addition, many of these studies have not looked at how accurately AERI retrievals depict common structures found in the boundary layer over the diurnal cycle, which is often critical to identifying the origins of conditionally unstable parcels. Filling these knowledge gaps may help reveal how AERIs and radiosondes may complement each other to create an improved diagnosis of the atmosphere.

To improve the understanding of AERI-retrieved profiles in environments supportive of deep, moist convection, this paper first offers a look at the accuracy of AERI-derived boundary layer profiles of temperature and water vapor over the diurnal cycle. After that, a comparison of the convection indices derived from the AERI instrument to those derived from radiosondes is performed. In section 2, we describe the AERI instrument and the retrieval algorithm used to derive the thermodynamic profiles from the AERI observations. In section 3, we describe the data and methods used to develop this comparison. In section 4, comparisons of the AERI profiles to radiosondes released over the diurnal cycle will reveal where the smooth nature of the AERI profiles may cause inaccurate representations of the true thermodynamic profile. Section 5 will assess the quality of the AERI-derived convection indices over the diurnal cycle compared with radiosondes and will compare the impact of instrument errors on the convection indices derived from the AERI and radiosonde instruments. The last section will summarize the overall accuracy of the AERI in these environments and make suggestions for how the accuracy can be improved.

2. Atmospheric Emitted Radiance Interferometer

a. Instrument description

The AERI is a ground-based remote sensor that measures downwelling infrared radiation between 520 and 3300 cm^{-1} (3.0–19.2 μm) at a resolution of 0.5 cm^{-1} (unapodized; see Knuteson et al. 2004a,b). Early versions of the AERI, such as those used in this study, record these observations at a frequency of every 7.5 min, whereas today's AERIs record observations every 20–30 s (Turner et al. 2016). AERI instruments maintain their calibration by regularly observing two blackbodies (one at 333 K and one at the ambient temperature) contained within the instrument housing. This calibration allows for a spectral accuracy better than 1% of the ambient radiance. The AERI can operate in clear and cloudy conditions, although the instrument's hatch automatically closes to protect the foreoptics of the instrument when precipitation is present.

b. AERIoe retrieval

Thermodynamic profiles have been retrieved from the AERI radiance spectra since the mid-1990s using a retrieval algorithm called AERIprof (Smith et al. 1999; Feltz et al. 1998). AERIprof has several limitations: 1) the carbon dioxide concentration was fixed and not easily changed, 2) the fast radiative transfer model used within AERIprof was tuned for Southern Great Plains (SGP) conditions and hence had significant errors when used in the tropics or Arctic, 3) uncertainty estimates are not provided by this algorithm, and 4) the algorithm was very sensitive to its first guess and thus was not able to converge to a solution in cloudy situations. This motivated the development of a new retrieval algorithm called AERIoe (Turner and Löhnert 2014) to address these shortcomings.

The AERIoe retrieval algorithm, which is a physically based iterative retrieval algorithm, uses the

optimal estimation (OE) framework (Rodgers 2000) that quantifies the uncertainty of the retrieved variables and the information content of the observations used in the retrieval. At its foundation, AERIoe utilizes portions of the AERI-observed spectral range that correspond to atmospheric windows and emissions of CO_2 and H_2O. AERIoe currently uses the line-by-line radiative transfer model (LBLRTM; Clough et al. 1992), version 12.2, to relate AERI observations to profiles of temperature T and water vapor mixing ratio q; this allows AERIoe to continue to use the latest spectroscopy by simply updating to a newer version of LBLRTM as needed. In addition, AERIoe retrieves cloud properties [e.g., liquid water path (LWP)], which enables the algorithm to provide thermodynamic profiles in both clear and cloudy conditions. As a Bayesian retrieval, AERIoe uses a priori estimates of the mean $\mathbf{X}_a$ and covariance $\mathbf{S}_a$ state of the atmosphere, which for this study was calculated from a 3-month radiosonde climatology generated using radiosondes regularly released at the ARM Southern Great Plains site (Sisterson et al. 2016).

The OE equation solves for variables [e.g., $T(z)$, $q(z)$, LWP] contained within a state vector $\mathbf{X}$ by iterating the following equation n times until the retrieval reaches some set convergence criteria:

$$\mathbf{X}^{n+1} = \mathbf{X}_a + (\gamma\mathbf{S}_a^{-1} + \mathbf{K}_n^{\mathrm{T}}\mathbf{S}_e^{-1}\mathbf{K}_n)^{-1}\mathbf{K}_n^{\mathrm{T}}\mathbf{S}_e^{-1}[\mathbf{Y} - F(\mathbf{X}^n) + \mathbf{K}_n(\mathbf{X}^n - \mathbf{X}_a)]. \quad (1)$$

Within this equation are the observation vector $\mathbf{Y}$, which contains observations such as the AERI spectra, and the forward model F. The Jacobian $\mathbf{K}$ describes the linear sensitivity of variables in the state vector to those in the observation vector. The final two variables, $\mathbf{S}_e$ and γ, are the error covariance of the observations and the retrieval stability parameter, respectively. Because of the highly nonlinear nature of infrared radiative transfer, γ is needed to stabilize the retrieval enough to reach convergence and is critical to overcome a poor first guess (which was one of the limiting factors of AERIprof).

The retrieval a posterior error covariance matrix $\mathbf{S}$ can be computed directly through the equations

$$\mathbf{S} = \mathbf{B}^{-1}(\gamma^2\mathbf{S}_a^{-1} + \mathbf{K}_n^{\mathrm{T}}\mathbf{S}_e^{-1}\mathbf{K}_n)\mathbf{B}^{-1} \quad (2)$$

and

$$\mathbf{B} = (\gamma\mathbf{S}_a^{-1} + \mathbf{K}_n^{\mathrm{T}}\mathbf{S}_e^{-1}\mathbf{K}_n). \quad (3)$$

Readers are referred to Turner and Löhnert (2014) and Blumberg et al. (2015) for a more detailed discussion of the AERIoe algorithm.

Turner and Löhnert 2014 have shown that the majority of the AERI's information content (>95%) is in the lowest 3 km. This limitation is problematic when using AERI profiles to understand deep, moist convection because large errors in the mid- and upper troposphere can translate into significant errors in the calculation of the convection indices. To overcome this problem, AERIoe has undergone substantial revisions to improve the quality of the entire retrieved tropospheric profile. In the latest version, AERIoe, version 2.2, surface layer observations and observations from additional sources of upper-air thermodynamic profiles (e.g., radiosondes, NWP forecast soundings, Raman lidar) can be included within $\mathbf{Y}$. The inclusion of NWP forecast soundings in the mid- to upper troposphere improves the overall retrieval as short-term forecast models are often most accurate at these altitudes (Thompson et al. 2003; Benjamin et al. 2004a,b). The intent of including these observations in AERIoe is to improve the retrieval in locations within the profile where the AERI spectra may lack information and therefore improve the algorithm's overall estimate of the entire tropospheric thermodynamic profile. When such observations are available, they are linearly interpolated to the AERIoe vertical grid and are treated in the algorithm as having perfect sensitivity (a value of 1) in $\mathbf{K}$.

3. Data and methods

a. Datasets and quality control

To investigate the performance of the AERI in convective environments, a dataset collected by five ARM observing facilities during the International H_2O Project 2002 (IHOP_2002; Weckwerth et al. 2004) was used (Fig. 1). IHOP_2002 ran from 13 May to 25 June 2002 and aimed to study the 3D distribution of water vapor and its relationship to precipitation. Each facility hosted an AERI instrument (Hackel et al. 1994), a Vaisala CL25 ceilometer (Ermold and Morris 1996), a Vaisala RS-90 radiosonde launch station (Kyrouac et al. 1994), and surface temperature, humidity, wind, and pressure sensors (THWAPS; Ermold and Kyrouac 1999). Throughout this field experiment, radiosondes were simultaneously released from all five sites at 3-h intervals, starting daily at 0200 UTC (2100 local time), resulting in a high temporal coverage of the atmospheric evolution, while AERI instruments were operated continuously.

Initially, there were 592 radiosonde profiles that were coincident with AERI observations. Prior to running the AERIoe retrieval, both the radiosonde and AERI data were screened for quality issues. First, comparisons between the AERI surface pressure sensors and the THWAPS data at all five sites found that the AERI pressure sensor was biased by 2–3 hPa. To correct for this, AERI surface pressure values used in AERIoe were replaced using the data from THWAPS. Second, as

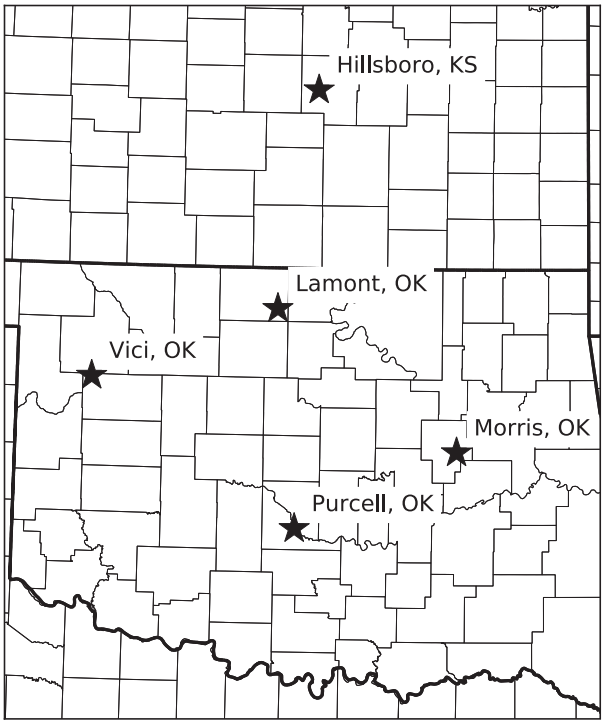

FIG. 1. Locations of the five ARM AERI observing facilities used during IHOP_2002.

clouds are relatively opaque in the infrared and thus hinder AERIoe from accurately retrieving the thermodynamic profile above cloud base, cloudy AERI spectra with an LWP greater than 6 g m^{-2} are not used in this study. AERI retrievals that did not converge or indicated a cloud were removed (166 profiles removed). This LWP threshold value corresponds roughly to an optical depth of 1; clouds with larger LWP values (and hence larger optical depths) have relatively small transparency, thus greatly limiting the AERI's ability to make meaningful measurements above the cloud (i.e., the information content above these clouds is relatively small). Last, radiosonde profiles were removed where the instrument's flight terminated below 10 km above ground level (AGL) or was found to have suspicious lapse rates (e.g., non-surface-based superadiabatic layers; 23 profiles removed). Any remaining radiosonde profiles were then linearly interpolated to the AERI 55-level-height grid to facilitate comparison to the AERI-retrieved profiles (sections 4 and 5d). This filtering process left 403 profiles for comparisons.

b. AERIoe configuration

AERIoe was only run on the AERI data collected nearest to the radiosonde launch time (roughly ±10 min relative to launch time). Retrievals were run using AERIoe, version 2.2, which utilized several different observation types to produce a best estimate of the tropospheric temperature and water vapor mixing ratio profile. Previous AERIoe analyses used only AERI radiances and cloud-base height from a collocated ceilometer as input; here, output from the Rapid Update Cycle (RUC) model (Benjamin et al. 2004a,b) and surface meteorology observations were also used as part of the retrieval. Table 1 summarizes the input data used in the **Y** vector of the AERIoe retrievals.

TABLE 1. Observations utilized in the **Y** vector in version 2.2 of the AERIoe retrieval. Superadiabatic layers were restricted in the retrieval to only the lowest 500 m of the thermodynamic profile. Noise values for AERI channels are described in Turner and Löhnert (2014) and Blumberg et al. (2015). The 1-σ observation errors listed for temperature T and water vapor mixing ratio q for the RUC and THWAPS shown are the median values for the entire dataset; z represents the heights over which these data are used in the retrieval.

AERI bands	20-km RUC	THWAPS
538–588 cm^{-1} 612–618 cm^{-1} 624–660 cm^{-1} 674–713 cm^{-1} 713–722 cm^{-1} 860.1–864.0 cm^{-1} 872.2–877.5 cm^{-1} 898.2–905.4 cm^{-1}	z = 4–18 km AGL σ_T = ~1°C σ_q = decreasing from 0.7 to near 0 g kg^{-1} over the altitudes from 4 to 18 km AGL	z = 2 m AGL σ_q = ~0.7 g kg^{-1} σ_T = 5 K

The AERI spectral bands used in AERIoe correspond to emission by carbon dioxide, water vapor, and cloud properties (Feltz et al. 1998; Löhnert et al. 2009; Turner and Löhnert 2014; Blumberg et al. 2015). These past studies have established that use of the channels listed in Table 1 in AERI retrievals results in a largely unbiased low-level (0–3 km) thermodynamic profile. Figure 2a illustrates an example AERI spectra highlighting the various channels listed in Table 1. To improve the information content and hence the accuracy of the temperature retrieved aloft, the less opaque 713–722-cm^{-1} carbon dioxide channels were included in the AERIoe retrieval. Figure 2b shows $\mathbf{Y} - F(\mathbf{X})$, where **Y** is the AERI channels highlighted in Fig. 2a used in an example AERIoe retrieval and $F(\mathbf{X})$ is the forward calculation of the retrieved state vector that was found using AERIoe. Although these channels could theoretically be extended further into the wings of the 15.0-μm CO_2 band to 770 cm^{-1} to provide an improved thermodynamic profile, it currently is not recommended. Experiments including these channels in the AERIoe retrieval have revealed inconsistencies between the LBLRTM and AERI that may be attributable to issues in the calibration of the AERI (and, in

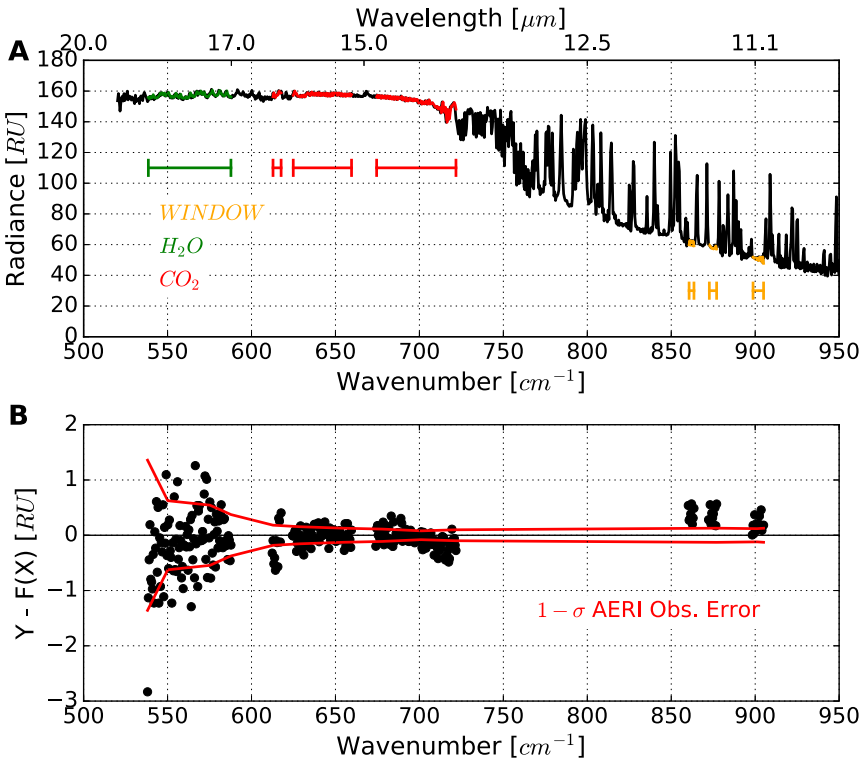

FIG. 2. (a) Sample AERI spectra from the Purcell, Oklahoma, AERI at 2334 UTC 12 Jun 2002 with portions of the spectra used in the AERIoe retrieval highlighted in orange, green, and red colors. (b) The residuals between the observed AERI spectra and the spectra calculated using the LBLRTM and the retrieved profile (see Fig. 3a). The red lines in (b) indicate the AERI 1-sigma observational error used in the retrieval. Here, 1 RU = 1 mW $(m^2\ sr\ cm^{-1})^{-1}$.

particular, the finite field-of-view correction; see Knuteson et al. 2004b) or the spectroscopy within the LBLRTM. The ceilometer provided information about the location of a cloud base in a manner similar to the method outlined in Turner and Löhnert (2014) and Blumberg et al. (2015).

Both surface meteorological observing systems and NWP profiles were used in the retrieval to improve the overall estimate of the tropospheric thermodynamic profile. For the surface meteorological observations, only water vapor mixing ratio values from THWAPS were used in the retrieval. A 1-sigma error of approximately 0.7 g kg^{-1} for q was used, which is roughly a 2%–3% error in relative humidity (RH; ARM Climate Research Facility 2011). A large error of $\sigma_T = 5$ K was used to reduce the influence of the THWAPS temperature measurement in the retrieval, as the AERI's spectra contain information about the surface temperature, and inconsistencies between the THWAPS measurement and AERI spectra can prevent AERIoe from converging. For the NWP profile, hourly 20-km RUC analysis files obtained through the ARM archive were used (Wagener et al. 2002; Benjamin et al. 2004a,b). From these files, both the vertical thermodynamic profile from the grid point nearest to the AERI location and a measure of the mesoscale spatial uncertainty of the profile were extracted. This spatial uncertainty was determined by calculating the 1-sigma standard deviation of each vertical point in the profile from a distribution of RUC profiles. This distribution was obtained by using a 200 km × 200 km horizontal space window centered on the AERI observation in space and time. Within AERIoe, this uncertainty was treated as the RUC model profile "observation error" within the retrieval $\mathbf{S}_e$ matrix. The 1-σ errors for RUC T and q values for the 4–18-km layer were roughly 1°C and between 0 and 0.7 g kg^{-1}, respectively. These uncertainties are similar to the magnitude of RUC errors found in Thompson et al. (2003). A similar method of calculating the uncertainty of the model profile for the AERIoe retrieval has been used by Bonin et al. (2015).

c. *Convection indices and parcel types*

Convection indices used in this study were calculated using the Sounding and Hodograph Analysis and Research Program in Python (SHARPpy; Blumberg et al. 2017),

version 1.3. SHARPpy is an open-source software package that is a direct rewrite of the sounding analysis routines managed and developed at the NOAA Storm Prediction Center. In the present study, only the indices CIN, CAPE, 500-hPa lifted index LI_5, and the buoyancy minimum B_{min} calculated from SHARPpy are evaluated. The B_{min} is the minimum buoyancy experienced by a parcel lifted from a specific height and is a relatively new index that has been shown to help understand how mesoscale thermodynamic processes destabilize parcels (Trier et al. 2014a,b, 2015). The B_{min} provides similar but less complete information compared to CIN and does not require vertical integration or the presence of an LFC. Three common parcel types are used in this study: the surface-based (SB) parcel, 100-hPa mixed-layer (ML) parcel, and the most unstable (MU) parcel. The MU parcel is found by determining the parcel with the highest equivalent potential temperature θ_e within the lowest 400 hPa of the sounding. All parcel-lifting calculations utilize the virtual temperature correction to account for the impact of water vapor on calculations of buoyancy (Doswell and Rasmussen 1994).

d. Calculating the uncertainty of convection indices

The method we use to calculate convection indices considers conditional stability in a probabilistic sense, per the recommendation in Moller (2001) that forecasters use parameter measures (e.g., CAPE) in a probabilistic manner. While accounting for sampling errors due to balloon drift on indices is beyond the goals of the present work, quantifying the impact of random and systematic errors on the calculation of each index is possible. We do this by using Monte Carlo sampling of the profile error covariance matrix $\mathbf{S}$ to produce a distribution of possible thermodynamic profiles. Parcels are then lifted in each profile to produce a distribution of convection indices. This distribution will allow for a comparison of the uncertainty inherent in the indices derived from both AERIoe and the radiosonde instrument.

To derive the distribution of indices from a single profile, each instrument's thermodynamic profile is Monte Carlo sampled 500 times using the equation

$$\hat{\mathbf{X}} = \mathbf{S}^{1/2}\mathbf{Z} + \mathbf{X}, \tag{4}$$

where $\mathbf{S}$ is the error covariance matrix for each measurement,[1] $\mathbf{Z}$ is a normally distributed random number with the same dimensions as the state vector, and $\hat{\mathbf{X}}$ is the perturbed profile. Parcels are lifted from each profile calculated from this method to calculate a distribution of convection indices. As distributions from convection indices with bounds (e.g., CAPE, CIN, and B_{min}) exhibit non-Gaussian behavior as they approach their bounds, the median and interquartile range (IQR) statistics are used to describe the central tendency and variability of each index. For the analyses in sections 5a, 5b, 5c, and 5e, the full 2-s-resolution profiles are used with this method to calculate the radiosonde convection indices.

4. AERI-derived boundary layer profiles

As the lower vertical resolution of the AERI may act as a hindrance in detecting destabilization trends in the atmosphere, it is important to understand how common boundary layer structures relevant to deep, moist convection (e.g., inversions) appear to the AERI. To do this, radiosonde profiles were separated into two datasets: convective boundary layer (CBL) profiles and stable boundary layer (SBL) profiles. CBL profiles were selected by first calculating the CBL top from the radiosonde potential temperature profile $\theta(z)$. The CBL top z_i was found by searching for the height where a surface parcel lifted dry adiabatically intersected with the original θ profile (Stull 1988). Profiles where z_i was above 300 m AGL were considered CBL profiles ($n = 206$). This threshold was determined subjectively by analyzing the individual radiosonde profiles to make sure that profiles included in the CBL category had a surface-based mixed layer. Profiles that did not meet these criteria were considered SBL profile candidates. These candidates were subject to a SBL top-finding algorithm. This algorithm started at 30 m AGL and iterated level by level until the temperature was no longer found to increase with height ($n = 119$). The choice to begin the search at 30 m AGL aimed to avoid utilizing the questionable near-surface temperature profiles (e.g., $\partial T/\partial z < 0\,\mathrm{K\,km^{-1}}$) discovered in nocturnal AERI profiles during this study. Profiles where the temperature did not increase with height were rejected from the SBL dataset (Stull 1988), and the final level h found by the algorithm was considered the SBL top.

To compare the CBL and SBL AERI retrievals with the radiosonde profiles, two datasets were created. The first dataset contained the interpolated 55-level radiosonde profiles $\mathbf{X}_{sonde}$, with both the AERI and radiosonde $\theta(z)$ and $q(z)$ profiles normalized by their determined radiosonde PBL top values (z_i, h). In the second dataset, the radiosonde profiles were smoothed using the averaging kernel $\mathbf{A}$ (see Turner and Löhnert 2014). The rows of $\mathbf{A}$ describe the smoothing of the retrieved thermodynamic profile as a function of altitude

[1] Creation of a radiosonde error covariance matrix is discussed in the appendix.

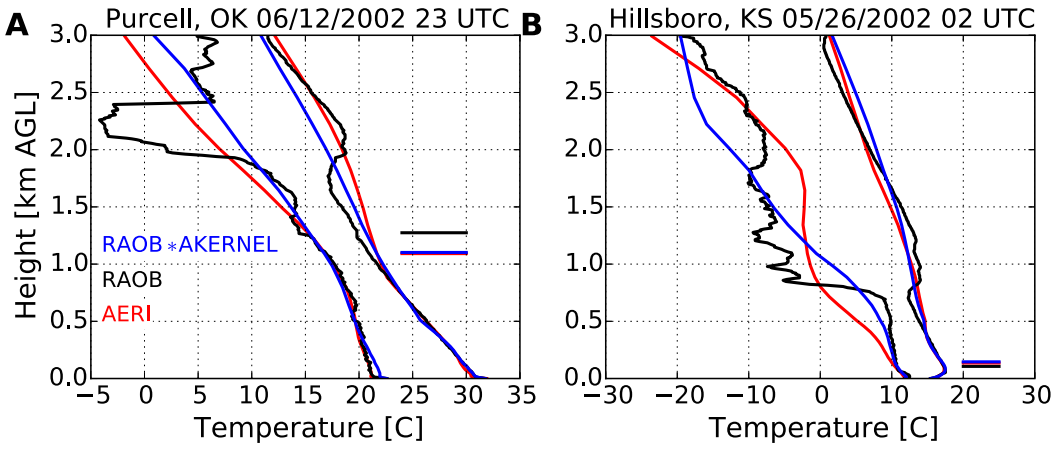

FIG. 3. Example soundings from the (a) CBL and (b) SBL datasets used in the study. Both the temperature and dewpoint profiles are shown from the AERI retrieval (red), the 2-s radiosonde (RAOB; black), and the RAOB profile smoothed by the averaging kernel (AKERNAL; blue). The black, red, and blue horizontal lines represent the PBL top locations from the unsmoothed radiosonde, AERI, and smoothed radiosonde, respectively. In (a), the RAOB × AKERNEL and AERI CBL top lines are nearly collocated with one another. In (b), all three estimates of the SBL top are close to one another.

that is caused by the level-to-level covariance described in the retrieval a priori dataset and the broad weighting functions of each channel used. Each smoothed radiosonde profile $\mathbf{X}_{\text{sonde}}^{\text{smoothed}}$ was calculated by the equation

$$\mathbf{X}_{\text{sonde}}^{\text{smoothed}} = \mathbf{A}(\mathbf{X}_{\text{sonde}} - \mathbf{X}_a) + \mathbf{X}_a. \quad (5)$$

These smoothed profiles were then normalized by the PBL top values determined from their unsmoothed profile. This second dataset was created to produce radiosonde observations that could be compared to the AERI profile that would demonstrate the impact of the AERIoe vertical resolution on accuracy. Figure 3 depicts the AERI and radiosonde comparison for two example soundings from the CBL and SBL datasets and illustrates how the averaging kernel acts to smooth the strong gradients present in the radiosonde profile.

a. Evaluation of AERI-derived CBL profiles

Figure 4 illustrates the AERI thermodynamic retrieval accuracy with respect to the CBL structure using the metrics of bias[2] (Fig. 4a), 1-sigma standard deviation (STD; Fig. 4b), and Pearson's correlation coefficient r (Fig. 4c). Within the lowest half of the CBL, the bias (Fig. 4a) is less than 0.5°C for potential temperature and 0.5 g kg^{-1} for water vapor mixing ratio, and the STD is 0.5°C and 0.7 g kg^{-1} (Fig. 4b), respectively. In addition, the r values are at a maximum in this lowest half, with $\theta(z)$ having a slightly larger r (~0.99) than $q(z)$ (0.97; Fig. 4c). However, as the profile approaches the top of the radiosonde CBL ($z/z_i = 1$), the AERI potential temperature profile exhibits a warm bias that peaks at the top of the CBL. Likewise, the water vapor mixing ratio profile develops a dry bias that nearly reaches 1 g kg^{-1} at the top of the CBL. This is because the AERI retrieval is unable to resolve the rapid change in the profile shape at the top of the CBL and therefore averages through the rapid changes instead (see Fig. 3a). The increases in bias near the top of the CBL are accompanied by increases of the potential temperature and water vapor mixing ratio STD to 1.4°C and 1.7 g kg^{-1}. Above the CBL top, the sign of the water vapor mixing ratio bias reverses, changing to a −0.7 g kg^{-1} moist bias but returns to nearly 0 g kg^{-1} at a height twice that of the CBL depth. The AERI $\theta(z)$ bias, however, returns quickly to 0°C immediately above the CBL top but exhibits a slight warm bias where $z/z_i = 3$. The $\theta(z)$ and $q(z)$ r value and STD reach their respective minimum and maximum just above the CBL top. The $\theta(z)$ profile exhibits a much smaller peak in STD and correlation coefficients compared to $q(z)$. These profiles do not decrease in accuracy with height above the CBL top because of the use of the RUC profile in the retrieval. It is important to mention that the r values shown in this study for the $q(z)$ profiles are much higher than those reported in Weckwerth et al. (2016). This is related to the temporal resolution of the comparisons; the Weckwerth et al. analysis used 5-min resolution, and thus, the changes in $q(z)$ with time were small relative to the AERIoe retrieval uncertainty, whereas in our study, the resolution of 3 h allows for much larger differences

[2] All errors are calculated as AERIoe − radiosonde.

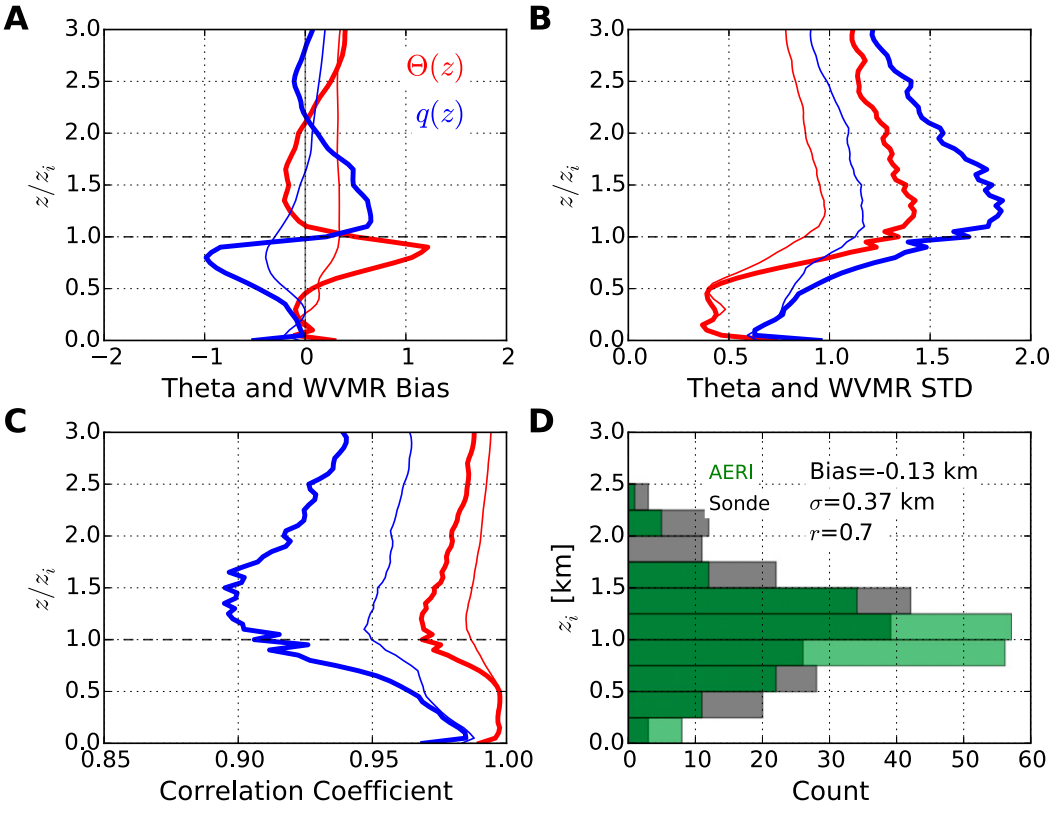

FIG. 4. (a) The AERIoe minus sonde θ (red; °C) and q (blue; g kg^{-1}) biases for CBL profiles. (b) AERI 1-sigma STD of the AERIoe minus sonde differences for those same profiles. (c) The correlation coefficient for each level in the normalized CBL profiles. (d) The distribution of CBL top values from the AERI (green) and the radiosonde (black) for this dataset. A y-axis value of 1 is the CBL top measured using the radiosonde data z_i. For (a), (b), and (c), the thinner lines are for the same variables and statistics but are for the comparison with radiosondes that have had the averaging kernel applied (n = 206), whereas the thicker lines are for the original radiosonde data.

in $q(z)$ with time. By using a lower temporal spacing in our validation dataset, the individual AERI–radiosonde data points used in calculating the correlation coefficient have a range of values varying far above the AERI retrieval noise and therefore produce a stronger linear relationship. The metrics in Fig. 4 overall suggest that on average, daytime AERI thermodynamic profiles are less accurate near the CBL interface than elsewhere in the profile.

The inaccuracies near the CBL interface are a consequence of the retrieval vertical resolution that results from the weighting functions broadening with height as well as the vertical level-to-level correlation imposed by the prior dataset (which is a critical constraint that allows AERIoe to converge). Figure 4 also depicts the bias, STD, and r profiles of the AERI when compared to radiosonde profiles that have been smoothed using the AERI averaging kernel. From these profiles, the large biases previously found in the $q(z)$ and $\theta(z)$ profiles above and below the CBL top are largely gone. In addition, the STD for these profiles no longer experiences a rapid increase as they approach the CBL top. Immediately above the CBL top, the STD profile with and without the application of the averaging kernel differ by nearly 0.5°C for the $\theta(z)$ profile and 0.5 g kg^{-1} for the $q(z)$ profile. For the r profiles, the application of the averaging kernel also removes much of the large vertical differences between the AERI and radiosonde with height, with the largest impact being in the $q(z)$ profile. These reductions in bias, STD, and increase in r support the idea that these inaccuracies in the AERI thermodynamic profile are largely due to the retrieval's vertical resolution.

These vertical-resolution issues also affect assessments of the CBL depth from AERIoe profiles. Figure 4d illustrates the distribution of CBL depth values calculated from AERIoe and radiosondes. AERI-retrieved values of the CBL depth are typically closer to the ground than radiosonde-observed values, differing by an average of 130 m. This result is due to the AERI warm bias just below the top of the radiosonde CBL, which would imply a shallower CBL depth than

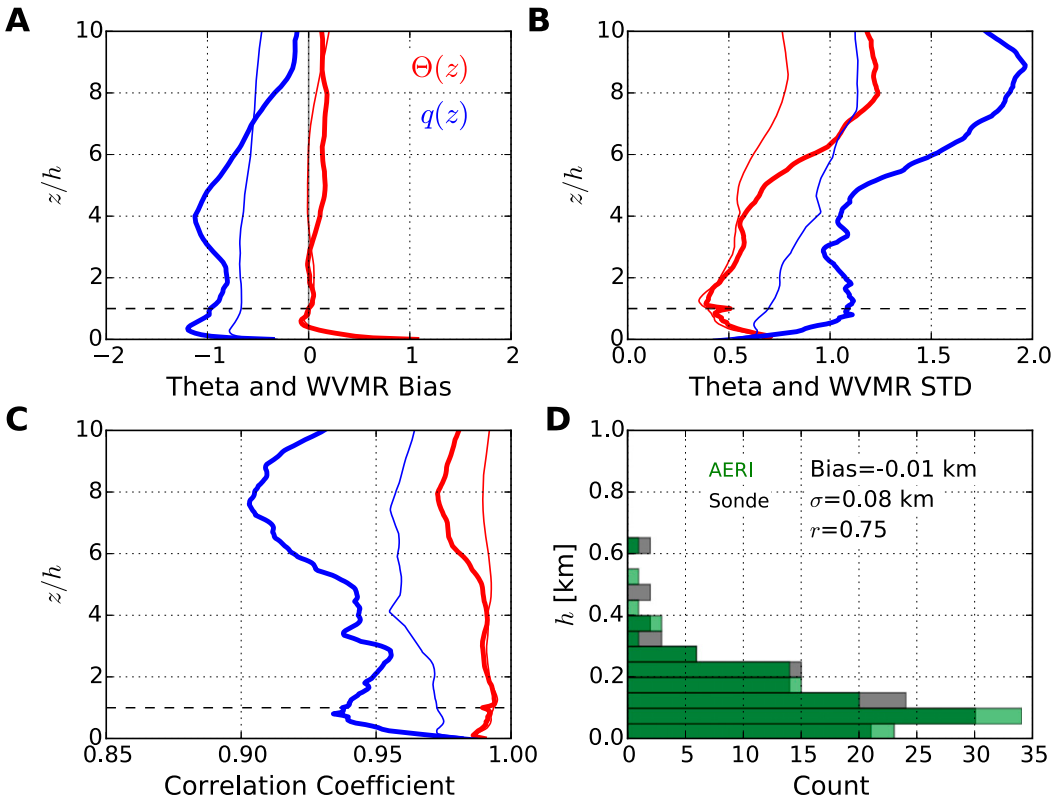

FIG. 5. As in Fig. 4, but for SBL cases. A z/h value of 1 represents the height of the surface-based inversion ($n = 119$).

observed by radiosondes, much like the example profile in Fig. 3a. In addition, the STD of the CBL depth errors for this dataset is found to be 370 m. AERIoe displays sensitivity to the radiosonde CBL depth values, with an r value of 0.7.

b. *Evaluation of AERI-derived SBL profiles*

Like the CBL, there are noticeable differences between the AERIoe and radiosonde profiles in bias, STD, and r in the SBL that can be attributable to how AERIoe represents the SBL profile (Fig. 5). Beneath the top of the SBL, AERIoe has a $\theta(z)$ warm bias that peaks at 1°C at the surface (Fig. 5a). This warm bias rapidly diminishes as the thermodynamic profile approaches the top of the SBL ($z/h = 1$) and remains largely unbiased with height until $z/h = 10$. Below the SBL top, the STD $\theta(z)$ profile is around 0.5°C. Above the SBL top and within the residual layer, the STD profile for potential temperature increases to 1.0°C (Fig. 5b). Although far above the SBL top, the $\theta(z)$ and $q(z)$ profiles are both unbiased, and water vapor dry biases on the order of $1\,\mathrm{g\,kg^{-1}}$ are present in much of the SBL profile. In addition, the water vapor STD experiences an increase from 1 to nearly $2\,\mathrm{g\,kg^{-1}}$ near the top of the residual layer ($5 \leq z/h \leq 10$). In Fig. 5c, maxima in r for both $\theta(z)$ and $q(z)$ occur between $0 \leq z/h \leq 5$, suggesting that the AERI is most sensitive to the thermodynamic properties of the air below the SBL top and within the residual layer.

As in the CBL case, application of the averaging kernel to the radiosonde data can reveal where a reduction in retrieval accuracy may be attributable to the retrieval's vertical resolution. Figure 5b shows that application of the averaging kernel decreases the $q(z)$ STD profile throughout the entire profile, suggesting that resolution issues play a large role in the accuracy of SBL $q(z)$. In particular, near the top of the residual layer ($5 \leq z/h \leq 10$), the $q(z)$ STD profile decreases nearly by $1\,\mathrm{g\,kg^{-1}}$ and r increases from 0.90 to 0.96 (Fig. 5c). For $\theta(z)$, a similar but smaller decrease in STD occurs. This decrease occurs largely where $z/h > 5$, suggesting that the retrieval inaccuracies occur because of the inversion often found at the top of the residual layer. The decreases in $q(z)$ bias with the application of the averaging kernel in Fig. 5a indicate that although the retrieval's vertical resolution does cause a dry bias in $q(z)$ above and below the SBL top, this bias is not completely explained by the retrieval's vertical resolution. Likewise,

TABLE 2. The verification statistics for different median thermodynamic indices from the CBL and SBL datasets for the initial temperature, dewpoint, and height of the SB, ML, and MU parcels. Shown are the number of data points *n*, bias, STD of the error, and the Pearson's correlation coefficient *r*. The origin height of the SB and ML parcels are not included, as this value is always the surface point for these parcel types.

	CBL profiles				SBL profiles			
	n	Bias	STD	*r*	*n*	Bias	STD	*r*
SB temperature (°C)	206	0.29	0.72	0.99	119	1.1	0.66	0.99
SB dewpoint (°C)	206	−0.5	1.0	0.97	119	−0.02	0.59	0.98
ML temperature (°C)	206	−0.26	0.54	0.99	119	−1.2	0.56	0.99
ML dewpoint (°C)	206	0.75	0.94	0.98	119	0.1	1.2	0.96
MU height (km)	206	−0.07	0.47	0.72	119	0.06	0.62	0.58
MU temperature (°C)	206	0.56	3.03	0.90	119	−0.13	3.12	0.84
MU dewpoint (°C)	206	0.41	2.48	0.93	119	−0.74	2.95	0.86

resolution issues do not completely explain the warm bias in $\theta(z)$ below $z/h = 1$, as application of the averaging kernel does not change the bias profile at all. These biases are difficult to explain given the data available. However, since studies using more recent AERI deployments have not reported these biases (e.g., Turner and Löhnert 2014; Bonin et al. 2015; Blumberg et al. 2015; Weckwerth et al. 2016), these biases are not generalizable across all AERI deployments. Reconciling these differences has been left for future work.

Unlike the CBL, the top of the SBL determined from the AERI-retrieved profile compares more favorably to radiosondes, since it is found much closer to the AERI instrument. This is indicated in Fig. 5d, as the AERI and radiosonde distributions of the SBL top are quite similar and biases between these values are on the order of 10 m. The STD value is 80 m, compared to 370 m in the CBL top cases (Fig. 4d). Last, this assessment shows that *r* values from the SBL comparison are slightly better than those in the CBL top comparison (0.7 vs 0.75).

5. Accuracy and uncertainty of thermodynamic indices

a. Parcel initial properties verification

The accuracy of AERI-derived indices (e.g., CAPE) is strongly dependent upon the instrument's ability to obtain accurate initial thermodynamic properties of ascending parcels. Table 2 indicates the bias, STD, and correlation coefficient for the parcel height, temperature, and dewpoint for the CBL and SBL cases before parcel ascent. For the SB parcel, the temperature and dewpoint exhibit warm and dry biases in both the CBL and SBL cases, similar to the surface biases indicated in Figs. 4a and 5a. Additionally, the STD of the errors for this parcel ranges between 0.59° and 1.0°C, peaking for the SB parcel dewpoint in the CBL cases. All values of the SB parcel have very high *r* values between 0.97 and 0.99. The high accuracy of the SB parcel properties (except for the warm bias in the SBL) are provided by the combination of THWAPS data and the information in the AERI spectra about the near-surface temperature profile in the AERIoe retrieval.

While the ML parcel verification in Table 2 shows STD and *r* values on the same order as the SB parcel, several counterintuitive biases appear. Most notable is the absence of an ML parcel dry bias in both the CBL and SBL cases, when in fact a dry bias would be expected given the boundary layer dry biases apparent in Figs. 4a and 5a. Instead, a moist bias is apparent in the ML parcel during the CBL cases, and in the SBL cases the ML parcel dewpoint is unbiased. These issues are a function of using an instrument with a much higher vertical resolution (radiosonde) to verify coarser-resolution retrievals (AERIoe). In the case of the water vapor profile, both profiles decay with height. However, inspection of the lowest 100-hPa profiles shows that the AERI water vapor decays more slowly with height than the radiosonde because of the vertical correlations that result from the AERIoe retrieval. This means that for the radiosonde, distributions of water vapor in the lowest 100 hPa are more likely to exhibit non-Gaussian behavior with tails toward drier values than AERIoe. This difference creates a moist bias in the AERIoe retrieval as the more detailed structure of the radiosonde pulls the radiosonde ML parcel toward drier values when an average is taken. In the SBL cases, where the ML parcel dewpoint is unbiased, the AERIoe profile is already biased in the dry direction. These resolution differences effectively create a cancellation of the errors. A similar explanation exists for why the AERI SBL ML parcel has a cool bias despite the presence of a near-surface warm bias (Fig. 5a), where warm tails in the distribution of lowest 100-hPa radiosonde potential temperature occur because of sharper inversions in the

TABLE 3. As in Table 2, but using the 55-level radiosonde profiles smoothed by the AERI averaging kernel.

	CBL profiles				SBL profiles			
	n	Bias	STD	*r*	*n*	Bias	STD	*r*
SB temperature (°C)	206	0.27	0.72	0.99	119	1.1	0.68	0.99
SB dewpoint (°C)	206	−0.18	0.78	0.99	119	−0.5	0.51	0.99
ML temperature (°C)	206	−0.02	0.22	0.99	119	0.07	0.19	0.99
ML dewpoint (°C)	206	−0.25	0.79	0.98	119	−1.01	0.82	0.98
MU height (km)	206	−0.01	0.32	0.81	119	0.18	0.48	0.67
MU temperature (°C)	206	0.01	2.54	0.92	119	−0.84	2.24	0.89
MU dewpoint (°C)	206	0.12	2.13	0.97	119	−0.52	2.76	0.89

radiosonde profile. These conclusions are reinforced by the recalculation of the biases of ML parcel properties using the smoothed radiosonde profiles created in section 4. This exercise recovers the expected signs of the biases in the CBL and SBL parcels (Table 3). However, the warm bias in the ML SBL is quite small, as the warm bias is present in the AERIoe retrieval near the surface occurs over a very thin layer compared to the entire 100-hPa layer used to compute the ML parcel properties.

The final parcel, the MU parcel, has lower *r* values and higher STD values (approximately 3°C) than the ML or SB parcels. This larger imprecision is caused often by SHARPpy identifying a different MU parcel in the AERIoe profile than the radiosonde profile; because of the AERIoe smooth profile, it can be difficult to obtain similar initial properties of the MU parcel when comparing to a highly structured radiosonde profile. This is evident where the MU parcel, although generally unbiased in the height of the parcel origin, has an STD of roughly 0.5 km and exhibits an *r* value less than 0.7 for the SBL and CBL datasets. Recalculation of these statistics using MU parcels found using the smoothed SBL radiosonde profile improves these metrics (STD = 0.19 km, $r = 0.67$ from STD = 0.62 km, $r = 0.58$). Given these results, thermodynamic indices derived from the SB and ML parcels should generally have a greater accuracy than those derived from the MU parcel.

b. *Thermodynamic indices verification*

Figure 6 shows the comparison between AERIoe and radiosonde for CAPE, CIN, LI_5, B_{min}, and the location of the buoyancy minimum (B_{min} height) indices. Table 4 describes verification statistics for this comparison; Fig. 6 illustrates the data used to calculate these statistics. These statistics and plots primarily demonstrate that the AERI retrieval is generally more accurate with indices that are only dependent upon differences at one vertical level, called nonintegrated indices (e.g., LI_5 and B_{min}) in the profile, rather than multiple levels through integration (e.g., CAPE and CIN).

The first example of this difference is apparent in how well the AERI measures two quantities that describe whether a parcel experiences positive buoyancy when lifted: the CAPE and LI_5 indices. Figure 6 demonstrates that the AERI retrievals may exhibit LI_5 errors between −2° and 4°C (Figs. 6d,i,n) and CAPE errors generally range between −1000 and 1000 J kg^{-1} (Figs. 6a,f,k). The AERIoe-derived LI_5 and CAPE values both have a bias relative to the radiosonde (Table 4), suggesting the AERI parcels have less instability (23.7–334.1 J kg^{-1}) than radiosonde parcels. This underestimation is primarily a function of the warm bias in the mid- to upper atmosphere visible at the top of Figs. 4a and 5a and is mitigated in the CBL ML and SBL SB parcels by their respective moist and warm biases discussed in section 5a. While both parcels are biased, LI_5 is still more accurate than CAPE. This is most apparent in the normalized STD (NSTD) metric, which is the ratio of STD to the 1-sigma standard deviation calculated using all the radiosonde indices for that index. For CAPE, the STD values range between 197 and 540 J kg^{-1}, and the NSTD is roughly 0.35–0.56. In contrast, the LI_5 STD for all parcels is bounded by 1.5°C and 0.24–0.31 for the NSTD values. Finally, the LI_5 variable has a larger *r* ($0.95 \leq r \leq 0.98$) than the CAPE quantities ($0.83 \leq r \leq 0.94$), suggesting that the AERI exhibits a stronger sensitivity to changes in LI_5 than CAPE. These results regarding the LI_5 index are similar to those found in Fig. 9 of Feltz et al. (2003), which used profiles retrieved from AERIprof (the older retrieval algorithm) to evaluate the AERI-derived LI_5 index to radiosondes. Overall, this comparison suggests integrated thermodynamic quantities (e.g., CAPE and CIN) derived from the AERI have a lower accuracy than nonintegrated quantities such as LI_5 and B_{min}.

Similar patterns arise when comparing the CIN and B_{min} variables. The differences between integrated and nonintegrated indices are best demonstrated in Table 4, where the SB and ML B_{min} correlation coefficients are larger than those for CIN. These differences do not hold

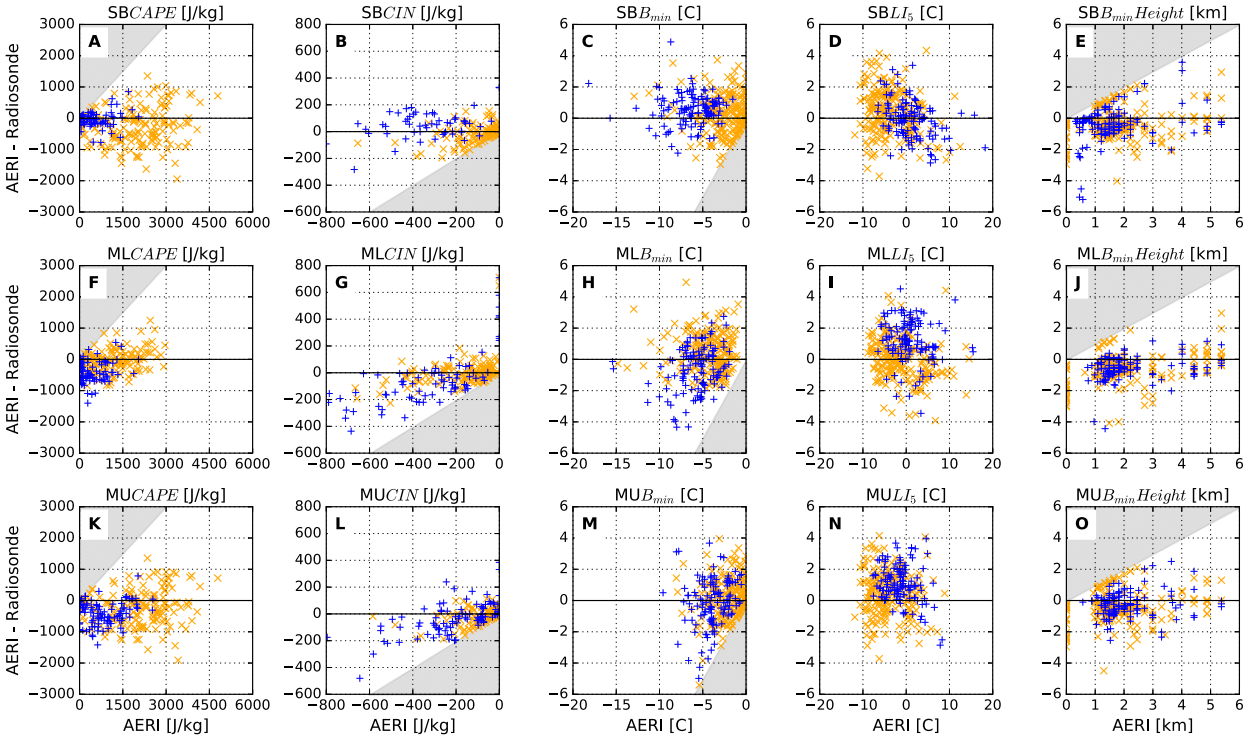

FIG. 6. Error plots for thermodynamic indices (a),(f),(k) CAPE (J kg^{-1}), (b),(g),(l) CIN (J kg^{-1}), (c),(h),(m) $B_{\min}$ (°C), (d),(i),(n) LI_5 (°C), and (e),(j),(o) $B_{\min}$ height (km) for the (top) SB, (middle) ML, and (bottom) MU parcels. The *y* axis represents the difference between the AERI and radiosonde index, while the *x* axis represents AERI index value. Blue points represent profiles from the SBL category, and orange points are from the CBL category. Light gray shading in the plots represents the area where invalid bias values exist because of a lower or upper bound on the range of valid index values (e.g., CAPE is nonnegative).

for the MU parcel, as the errors associated with obtaining the MU initial parcel properties described in section 5a play a significant role. Figures 6b,g,l show that CIN errors range largely between −200 and 100 J kg^{-1}, while $B_{\min}$ generally exhibits errors between −2° and 2°C (Figs. 6c,h,m). For all parcel types, large biases (from 50 to −58 J kg^{-1}) and STD values exist for the CIN values (51–200 J kg^{-1}). In comparison, the $B_{\min}$

TABLE 4. As in Tables 2 and 3, but for the different thermodynamic indices CIN (J kg^{-1}), CAPE (J kg^{-1}), $B_{\min}$ (°C), LI_5 (°C), and $B_{\min}$ height (km). NSTD is the ratio of STD to the 1-sigma STD calculated using all the radiosonde indices for that index. Only profiles where the radiosonde parcel being evaluated had a CAPE > 100 J kg^{-1} and a CIN > −800 J kg^{-1} were used in the CIN comparisons to ensure that the radiosonde had a nonzero value of CIN and CAPE.

	CBL profiles					SBL profiles				
	n	Bias	STD	NSTD	*r*	*n*	Bias	STD	NSTD	*r*
SB CAPE	206	−200.7	540.7	0.40	0.92	119	−23.7	197.6	0.40	0.92
SB CIN	158	−9.2	57.9	0.61	0.83	55	51.2	99.8	0.61	0.82
SB $B_{\min}$	206	0.3	1.2	0.46	0.88	119	0.6	0.9	0.34	0.94
SB LI_5	206	0.42	1.5	0.29	0.96	119	−0.1	1.2	0.24	0.98
SB $B_{\min}$ height	206	−0.4	0.9	0.71	0.72	119	−0.4	1.2	0.84	0.59
ML CAPE	206	−24.3	291.9	0.35	0.94	119	−265.5	333.9	0.56	0.83
ML CIN	131	−0.7	106.7	0.73	0.73	74	−48.8	200.3	1.18	0.49
ML $B_{\min}$	206	0.4	1.2	0.45	0.89	119	−0.6	1.4	0.60	0.81
ML LI_5	206	0.0	1.3	0.25	0.97	119	1.2	1.3	0.30	0.95
ML $B_{\min}$ height	206	−0.6	0.9	0.69	0.77	119	−0.6	0.8	0.62	0.79
MU CAPE	206	−183.4	518.7	0.39	0.92	119	−334.1	364.2	0.47	0.89
MU CIN	162	−10.0	51.1	0.61	0.84	93	−29.7	120.9	0.91	0.69
MU $B_{\min}$	206	0.2	1.3	0.65	0.77	119	0.13	1.5	0.73	0.70
MU LI_5	206	0.45	1.4	0.31	0.95	119	1.1	1.2	0.31	0.95
MU $B_{\min}$ height	206	−0.5	0.9	0.72	0.71	119	−0.3	0.8	0.69	0.72

index is unbiased and has STD values around 1.2°C, except in cases where the initial parcel values are biased (e.g., the SBL MU and ML parcels). In addition, CIN errors are larger than those from B_{min} as the NSTD values for CIN are greater than those for B_{min}. This is particularly true in the SBL and CBL cases with the ML and SB parcels. These results suggest that B_{min} is a better tool than CIN for assessing the strength of capping inversions with AERI-retrieved profiles since CIN values require accurate measurements of the entire layer exhibiting negative buoyancy, which AERIoe struggles to resolve fully.

Given that B_{min} values derived from AERIoe compare well to those from radiosondes, it is important to consider if both AERIoe and the radiosonde also identify similar locations of B_{min}, which is represented by the variable designated as "B_{min} height." Figures 6e, 6j, and 6o show the verification of the B_{min} height values from AERIoe and suggest that although AERIoe cannot precisely identify the same B_{min} height as the radiosonde, it is roughly able to capture the correct B_{min} height within the lowest 3 km of the profile. Above 2.5–3 km, where AERIoe vertical resolution in the thermodynamic profile decreases sharply (Turner and Löhnert 2014; Blumberg et al. 2015), errors of the B_{min} height estimation increase. Table 4 suggests that the STD of the B_{min} height ranges from 0.8 (SBL ML) to 1.2 km (SBL SB). Notable is that the r for the B_{min} height index ($0.59 \leq r \leq 0.79$) is occasionally lower than CAPE, LI_5, and B_{min} in Table 4. The outliers in Figs. 6e, 6j, and 6o (e.g., the points that lie along the gray shaded area or where the AERI $B_{min} = 0$°C) drive much of the decrease in accuracy evident in Table 4. The r statistic is strongly influenced by the presence of weakly capped environments (B_{min} approaches 0°C) within the dataset. In these environments, B_{min} height may jump from the parcel origin height to a different location aloft. There, small differences in the thermodynamic environment measured by AERIoe and the radiosonde may change the location of B_{min} significantly, and these can cause large differences between what each instrument considers the correct location of B_{min}.

Qualitatively, AERIoe-derived B_{min} height values occur at expected locations within the thermodynamic profile. For the CBL cases, more than 95% of AERI B_{min} height values in Figs. 6e, 6j, and 6o lie above the radiosonde CBL top. This location (roughly 1.5–3 km AGL) is where the capping inversion that often suppresses deep, moist convection in the Southern Great Plains is often found. A similar result occurs in the SBL cases. However, the distribution of SBL B_{min} height values have a bimodal distribution (Figs. 6e,j), with some B_{min} height values near the surface-based inversion (<1 km AGL) and others near the top of the residual layer (>1 km AGL), where the previous day's CBL top is found. Furthermore, evaluation of individual profiles suggests that the AERI largely identifies B_{min} height near layers where the radiosonde observes static stability increases. This suggests that rather than precisely identifying capping inversions, B_{min} height derived from AERIoe profiles may assist in the identification of layers where capping likely exists.

c. *Thermodynamic index random errors*

The impact of random and systematic errors on the calculation of convection indices from both AERIoe and radiosonde profiles was also evaluated. To do this, the IQR was computed from each distribution of convection indices generated via Monte Carlo sampling (section 3d) calculated for every clear-sky SBL and CBL AERI and radiosonde profile. The results from each instrument are illustrated in Fig. 7.

Within Fig. 7, several trends are apparent regarding the random errors from radiosondes and AERIs. First, the random errors for all indices do not seem to be strongly dependent upon parcel type. Second, for CIN, LI_5, and B_{min}, the random errors from the radiosonde are generally less than those from the AERI; however, the differences are quite small. Last, for indices that have a bound of 0 (e.g., CIN, CAPE, and B_{min}), the IQR narrows as the index values approaches that bound, causing the data points in Fig. 7 to curve toward 0, a behavior not captured by the trend lines.

For both instruments, the random errors for CAPE increase as the parcel instability grows (Figs. 7a,e). This behavior occurs for different reasons. First, it is important to note that large errors in parcel q often translate into large errors in CAPE. Second, for the Southern Great Plains, parcel q is often proportional to CAPE. For the AERIoe retrievals, as q increases, some AERI spectral channels become more opaque and decrease the overall degrees of freedom of signal (DFS), therefore increasing the q uncertainty in the AERIoe-retrieved parcel (Turner and Löhnert 2014, their Fig. 7). For the radiosonde, a 1% perturbation in RH in a high q environment translates to a much larger error of q than the same RH error in a low q environment. This reasoning explains why the precision of AERIoe and radiosonde instability measurements decreases as parcel instability increases. However, it is apparent from Fig. 7 that there are instances in which CAPE values measured by AERIoe have twice the precision of CAPE values from radiosondes. This occurs in profiles with CAPE values greater than 2000 J kg^{-1}, which is roughly where uncertainties in parcel q for the AERI become less than those for the radiosonde. These results indicate

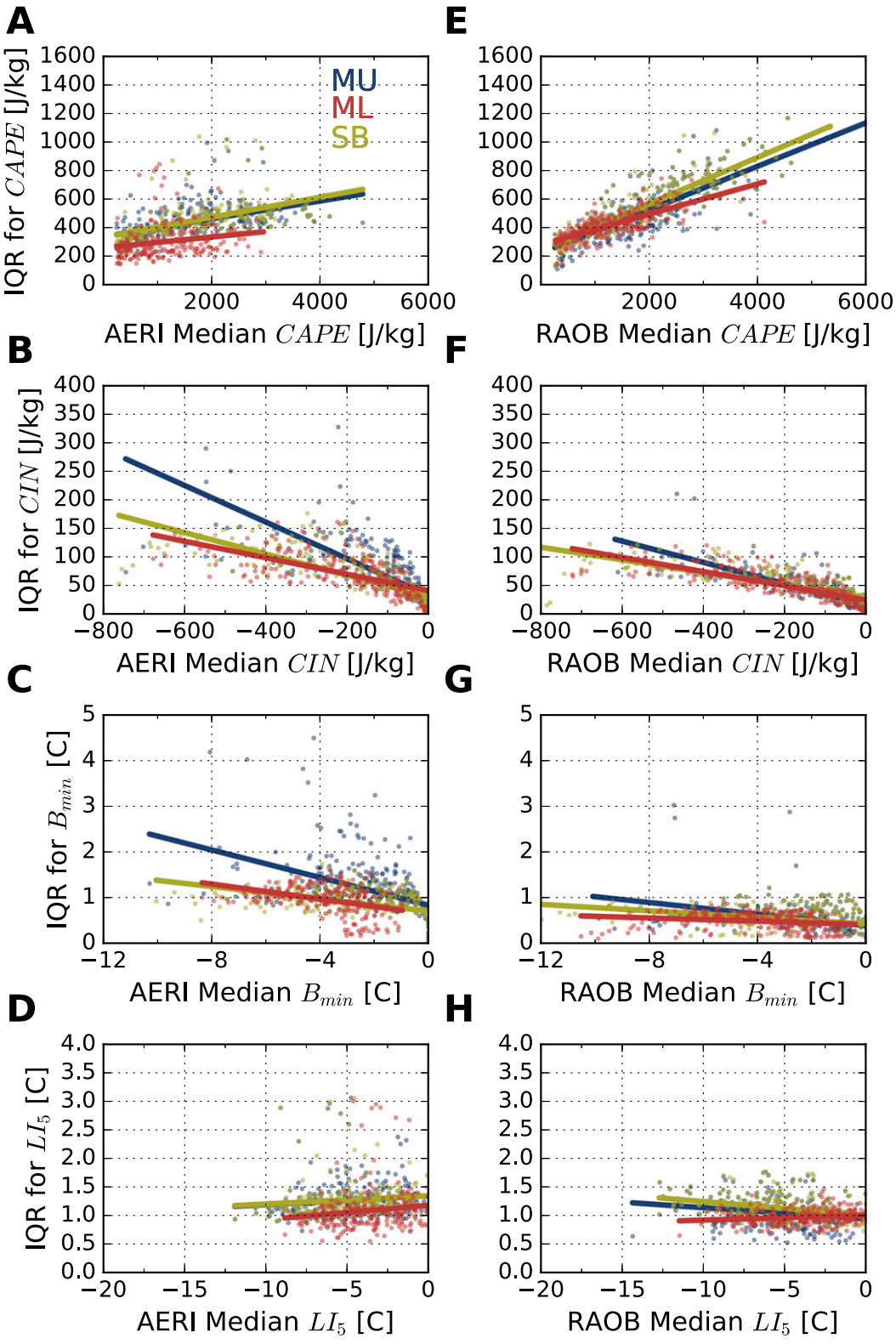

FIG. 7. The impact of instrument random error on the calculation of the CAPE, CIN, $B_{\min}$, and LI_5 indices using (a)–(d) AERI and (e)–(h) radiosonde profiles with CAPE $> 250\ \mathrm{J\ kg^{-1}}$. The IQR of the index distribution is on the y axis, while the median value of the index is on the x axis. The points are colored by the type of parcel used to calculate the index (MU parcel: blue; ML parcel: red; SB parcel: yellow). Thick lines indicate the line of best fit to qualitatively show the trends for illustration purposes.

that for very unstable environments, AERI calculations of CAPE are more precise than those from radiosondes. Additional tests (not shown) increasing the RUC σ_T to nearly 2°C in the AERIoe retrieval also seem to suggest that this conclusion holds for different RUC uncertainties.

d. Profiles of parcel stability

To test the AERIoe's capability to identify conditionally unstable layers of air, parcels were lifted from every level in the lowest 4 km of the CBL and SBL profiles. Unlike before, Monte Carlo sampling was not performed to generate indices from these parcels in order to simplify the comparison. From these parcels, profiles of $LI_5(z)$, $B_{min}(z)$, and B_{min} height(z) were created, where z is the height coordinate normalized with respect to the profile's radiosonde CBL or SBL top.

Figure 8 evaluates these AERI-derived thermodynamic index profiles for the CBL and SBL. This figure shows that for the CBL, $B_{min}(z)$ and B_{min} height(z) are largely unbiased throughout the entire profile (Fig. 8a). The AERI-derived $LI_5(z)$ profile within the CBL exhibits less buoyancy than the radiosonde, especially near the CBL top where the warm bias due to the smoother profile plays a larger role. For the STD profiles, the B_{min} height(z) largely does not vary much with height. However, the $B_{min}(z)$ and $LI_5(z)$ STD profiles start near 1.5°C and increase to nearly 2.5°–3°C at the CBL top. Figure 8b shows that the sensitivity of the AERI for all three profiles drops off at the CBL top. In the case of B_{min} height(z), the near-surface correlation coefficient drops off to 0.7, as cases where weakly capped environments and subtle differences in the AERI and radiosonde measurements cause differences where one instrument finds the B_{min} at the parcel origination level while the other finds it at the capping inversion. This same issue occurs with the low near-surface correlation coefficient in the SBL cases (Fig. 8d). Although the three convection parameters are uniformly accurate with height in this case, the most unstable parcels are found close to the surface, per the box-and-whisker plot in Fig. 8a.

The variations of accuracy with height of these indices within the SBL, although largely similar in STD and correlation coefficient to the CBL, do exhibit some differences. Most noticeable are the biases in B_{min} (nearly −1°C) and LI_5 (1°–2°C). These are largely due to the biases discussed in section 4b regarding how AERIoe depicts the SBL. However, these issues do not create any noticeable biases in the profile of the height of B_{min}. For B_{min} and LI_5, the STD profiles follow similar shapes to the CBL profile, where the errors increase near the CBL top and the residual layer top. In Fig. 8d, the B_{min} and LI_5 exhibit high correlation coefficients below the surface-based inversion, as AERIoe has enough information to resolve the inversion and the thermodynamic characteristics of the air below it. The AERI exhibits a layer of high r values for all three variables between the residual layer top and surface-based inversion height. This is beneficial, as the radiosonde MU parcels are often found within this layer per the box-and-whisker plot in Fig. 8c. In fact, Figs. 8c and 8d suggest that for the AERIoe retrieval in this layer, the error characteristics of the indices are roughly independent of parcel origin height. Overall, these properties suggest that even if the heights of the AERI and radiosonde SBL MU parcels were identical, the error characteristics of MU B_{min}, LI_5, and B_{min} height largely may not improve.

e. Accuracy of AERI 3-h stability trends

As both the AERI retrievals and radiosonde instruments may be used together to assess the evolution of parcel stability, we attempted to identify how often the two instruments may provide similar 3-h trends. Because the previous sections revealed that different characteristics of the AERIoe and radiosonde profiles make a comparison of the indices calculated from each instrument nontrivial, the trend of the indices may be more useful to consider when comparing the measurements from each instrument. To do this, all clear-sky retrievals and radiosonde data were sorted to isolate 3-h periods that contained AERIoe and radiosonde profiles at the beginning and end of the period ($n = 249$). Using the Monte Carlo–generated distribution of thermodynamic indices from each instrument, a dataset comparing the 3-h differences of the indices was developed. From this dataset, the frequency of events where AERIoe and radiosonde profiles measured a similar signed trend of the 3-h period was calculated. It is important to emphasize that this test attempts to account for the effects of instrument errors on the trend assessment and that this test uses only two discrete measurement points in time to approximate the trend, as 3 h is the maximum temporal resolution of the radiosonde dataset. This analysis does not account for any variability within the 3-h window measured by the AERI, as subscale variability (e.g., a thunderstorm passing by) within the window may cause an inaccurate assessment of the overall mesoscale trend.

Figure 9 illustrates the results from these tests for these different thermodynamic quantities. For most quantities tested, the AERI roughly detects the same signed trend as the radiosonde at least 60%–70% of the time. Additionally, the stronger the change in the index, the more likely the AERIoe retrievals are to match that

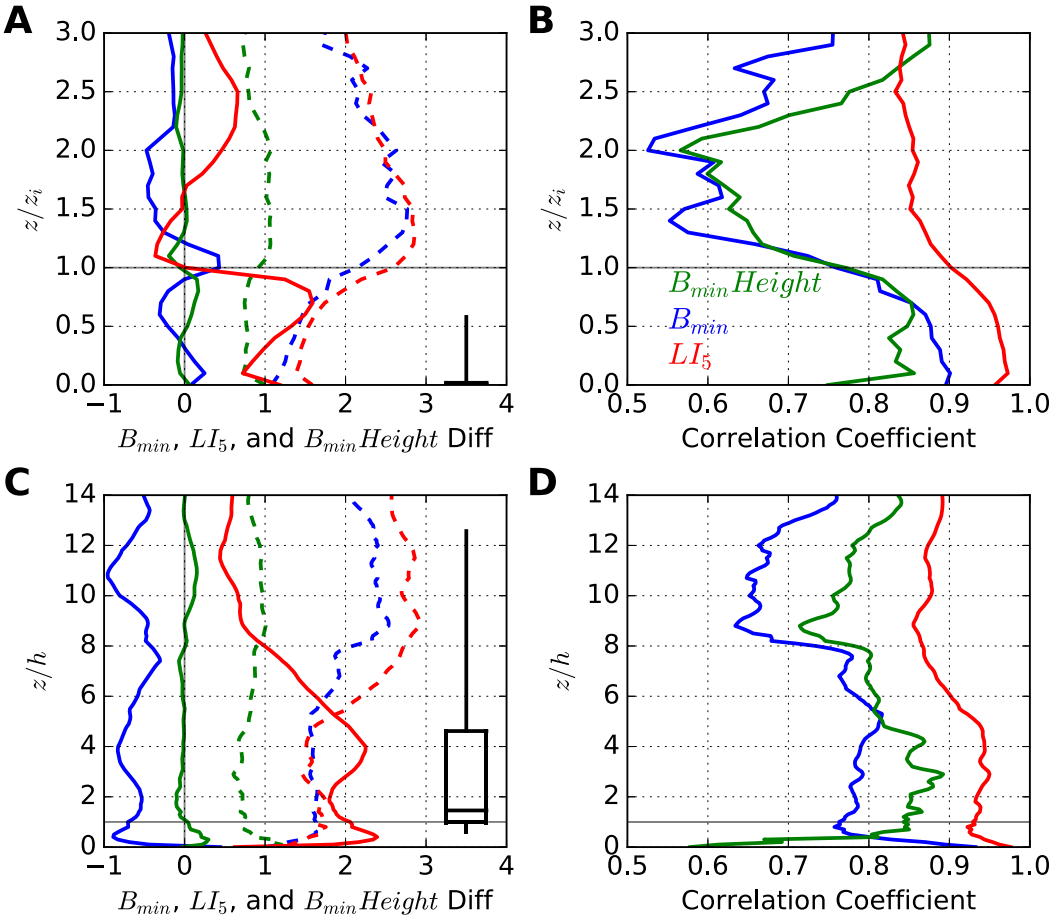

FIG. 8. Verification metrics for (a),(b) CBL and (c),(d) SBL 0–4-km $LI_5(z)$ (°C; red), $B_{min}(z)$ (°C; blue), and B_{min} height(z) (km; green) profiles. (left) The profile bias (solid) and STD (dashed) normalized by the SBL and CBL tops. (right) The correlation coefficient with height profile with the same normalization. The box-and-whisker plots in (a) and (c) display the distribution (10th, 25th, 50th, 75th, and 90th percentiles) of radiosonde MU parcel locations in each boundary layer category.

trend. For CAPE, the probability of detecting the correct trend increases from 75% to 90% between 0 and 1000 J kg^{-1}. A characteristic of Fig. 9 is that the SB parcel has a larger probability than the MU and ML parcels. This is especially apparent in Fig. 9e, where the detection of LCL trends is strongly dependent upon parcel type. This is because the SB parcel quantities are retrieved using AERI spectra and surface met tower data, both of which are highly sensitive to the thermodynamic characteristics of the near-surface air.

Figure 9 also suggests that when it comes to monitoring stabilization trends, AERIoe may detect changes in the parcel properties more readily than changes to the environmental thermodynamic profile. Figure 9f shows that, for all parcel types, AERIoe profiles may more reliably detect parcel θ_e changes than those in the environmental temperature (Fig. 9c). For example, a 4°C trend in θ_e has a chance $> 80\%$ of being detected by both the instruments, while a change in the height of B_{min} may be correctly detected with a probability of 50%–60%. This difference suggests that the AERI's primary benefit when assessing destabilization may be identifying changes to the initial parcel properties rather than precise changes in the environment, such as the lifting of a capping inversion. This is useful given that some of the dramatic changes in parcel instability are associated with an increase in moisture of the low levels rather than a change in environmental lapse rate (Markowski and Richardson 2007, 187–189). However, destabilization caused by changes to the environment viewed through the lens of AERIoe may be better identified via a general cooling with time aloft. This aspect of the AERI suggests that while the AERI may offer good insight into the general trends of convective stability, more detailed diagnoses of environmental changes may be necessary via radiosondes.

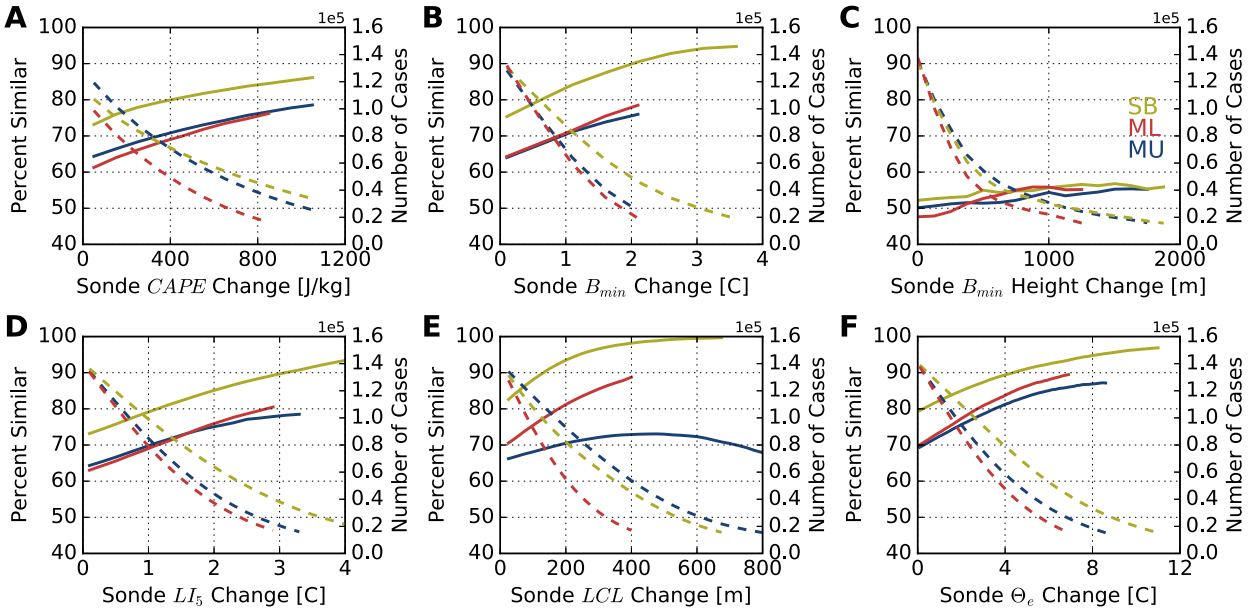

FIG. 9. An assessment to evaluate the percentage of the time the AERI and RAOB instruments indicate a similar trend sign (positive or negative) over a 3-h period. Indices shown are (a) CAPE, (b) $B_{\min}$, (c) $B_{\min}$ height, (d) LI_5, (e) LCL, and (f) parcel θ_e for different change thresholds (x axis). Solid lines indicate the percent of the time that similar trends were identified (left y axis) by the two instruments, and dashed lines represent the number of cases in each category (right y axis: $\times 10^5$). Blue lines indicate the MU parcel ($n = 233$), red lines indicate the ML parcel ($n = 192$), and yellow lines indicate the SB parcel ($n = 203$). Lines are truncated once the sample size decreases below 30 (15 000 given the Monte Carlo sampling).

6. Conclusions

Using 3-hourly radiosondes and AERI observations during IHOP_2002, this paper analyzed several different capabilities of the AERI instrument in environments supportive of deep, moist convection. First, comparisons with radiosondes show that the smooth AERI-retrieved profiles exhibit large inaccuracies primarily near the CBL interface and at the top of the SBL residual layer. Second, while these inaccuracies affect the accuracy of integrated indices such as CIN and CAPE, they largely do not impact simpler indices such as $B_{\min}$ and LI_5. Additionally, although the height of $B_{\min}$ derived from the AERI retrievals may vary compared with radiosondes, the level often occurs in regions of the profile where deep, moist convection is often suppressed (e.g., CBL and residual layer capping inversions) and somewhat subtle AERIoe-measured increases in static stability that deviate from well-mixed layers may occur. Third, propagation of random and systematic errors from the radiosonde and AERI retrievals through SHARPpy revealed that convection indices derived from the AERI tend to have uncertainty magnitudes slightly greater than radiosondes. However, for profiles in environments exhibiting large convective instability (CAPE $\geq 3000\,\mathrm{J\,kg^{-1}}$), CAPE measurements from AERIoe have nearly twice the precision that radiosondes do. Last, this study demonstrates that the AERI is primarily suited to monitor trends in parcel moist static energy and suggests that the AERI can capture destabilization trends. However, a more detailed understanding of why those trends are occurring (e.g., lifting of a capping inversion) may need to be augmented by radiosondes. Although the vertical resolution of the AERI retrievals may sometimes hinder a precise identification of capping inversions, such issues are overcome in environments where strong vertical gradients and rapid temporal changes occur in the thermodynamic profiles. This feature is particularly favorable for operational meteorologists working challenging convective forecasts with the potential for the rapid erosion of a strong capping inversion.

Three issues hinder the argument that these results are generalizable to all AERI deployments. First, this study focuses solely on the convective season in the central United States. Strong vertical contrasts in moisture and temperature (e.g., thermodynamic properties of the CBL and the elevated mixed layer; Carlson 1998) and rapid temporal changes in stability and moisture occur in these environments (e.g., the nocturnal low-level jet). This study suggests that given such environments, the AERI may offer useful guidance regarding the problem of nowcasting deep, moist convection in the U.S. Southern Great Plains. Additional studies similar to this one are needed in other

environments that do not exhibit such strong spatiotemporal contrasts to assess the AERI's usefulness in other climatic regions. Second, a warm and dry bias was identified in the SBL AERI profile that has not been reported in past studies using more recent AERI deployments. Last, this study utilized technology from 2002 in the AERIoe algorithm. AERIoe retrievals using noise-filtered AERI spectra (Turner et al. 2006) or more modern NWP tropospheric profiles should be more accurate than the retrievals found in this study and should better detect changes to capping inversions. Future studies could also use satellite radiances (e.g., Ho et al. 2002; Ebell et al. 2013) or lidar data (Barrera-Verdejo et al. 2016) within the AERIoe retrieval to improve the mid- to upper-tropospheric thermodynamic profile and facilitate an observation-only comparison to radiosondes. Additionally, literature suggests that inclusion of lidar (e.g., Raman lidar) data in AERIoe should have an added benefit of improving the vertical resolution of the retrieved profile (Barrera-Verdejo et al. 2016).

An important consequence of this study is that we have established a methodology for quantifying the uncertainty of convection indices due to measurement errors using a single radiosonde or OE-retrieved profile. Given the size of convection index errors possible in observed thermodynamic profiles, these results strongly suggest that a probabilistic approach should be used when calculating convection indices and doing so can assist in the intercomparison of indices. However, as this study has shown, measurement characteristics (e.g., vertical resolution) can sometimes create noticeable, systematic differences in convection indices even down to the initial parcel property calculations (section 5a), which on the surface may seem troubling. It is important to remember that while indices can be rooted in physical reasoning (e.g., parcel theory), they also often have a statistical or anecdotal component (e.g., studies tying indices from proximity soundings to phenomena) that assists in the interpretation of an index value. Because of this additional component, the assumptions inherent in the sounding data used in studies that clarify how to interpret a particular index may be violated when that index is transferred to a new instrument or data type; this may result in an invalid interpretation of the index. This issue suggests that while intercomparisons of indices between instruments are an important exercise, studies demonstrating relationships of AERI-derived indices to physical phenomena are also needed.

Acknowledgments. This work was partially supported by the U.S. Department of Energy Atmospheric System Research (ASR) program via Grant DE-SC0014375 as well as support from the director of the Cooperative Institute for Mesoscale Meteorological Studies (CIMMS) at the University of Oklahoma. The authors thank the ARM staff for maintaining the ARM boundary facilities throughout the IHOP campaign. This study would not be possible without the staff providing the high-frequency radiosonde launches over the diurnal cycle. We also thank Giri Prakash, Anthony Clodfelter, and David Sill for maintaining and troubleshooting the ARM bds2-vm1 machine at Oak Ridge National Laboratory, which was used for all data processing in this study. Last, we thank the three anonymous reviewers for their comments and suggestions.

APPENDIX

Developing the Radiosonde Error Covariance Matrix

Observation error covariance matrices were constructed using Vaisala RS-90 radiosonde instrument errors provided by the ARM program (Holdridge et al. 2011; Table 3). Two types of errors were considered: repeatability errors (random errors: $\sigma_{\mathrm{RH}} = 1.41\%$ RH, $\sigma_T = 0.39°\mathrm{C}$) and reproducibility errors (systematic errors: $\sigma_{\mathrm{RH}} = 3\%$ RH, $\sigma_T = 0.2°\mathrm{C}$). Each profile $T(z)$, $\mathrm{RH}(z)$ was perturbed by adding one randomly chosen systematic error value and a random noise profile; these perturbations were applied independently to T and RH. After converting the perturbed $T(z)$, $\mathrm{RH}(z)$ profiles into water vapor mixing ratio space, the covariance matrix $\mathbf{S}$ was calculated using the $T(z)$, $q(z)$ profiles. This matrix has off-diagonal values since the assumed uncorrelated errors in T and RH created correlated errors when calculating q, as both T and RH are independent variables in the equation used to compute q.

REFERENCES

ARM Climate Research Facility, 2011: Temperature, humidity, wind, and pressure system handbook. ARM Climate Research Facility Rep. ARM-TR-030, 12 pp., https://www.arm.gov/publications/tech_reports/handbooks/thwaps_handbook.pdf.

Barrera-Verdejo, M., S. Crewell, U. Löhnert, E. Orlandi, and P. Di Girolamo, 2016: Ground-based lidar and microwave radiometry synergy for high vertical resolution absolute humidity profiling. *Atmos. Meas. Tech.*, **9**, 4013–4028, doi:10.5194/amt-9-4013-2016.

Benjamin, S. G., and Coauthors, 2004a: An hourly assimilation–forecast cycle: The RUC. *Mon. Wea. Rev.*, **132**, 495–518, doi:10.1175/1520-0493(2004)132<0495:AHACTR>2.0.CO;2.

——, G. A. Grell, J. M. Brown, T. G. Smirnova, and R. Bleck, 2004b: Mesoscale weather prediction with the RUC hybrid isentropic–terrain-following coordinate model. *Mon. Wea. Rev.*, **132**, 473–494, doi:10.1175/1520-0493(2004)132<0473:MWPWTR>2.0.CO;2.

Blumberg, W. G., D. D. Turner, U. Löhnert, and S. Castleberry, 2015: Ground-based temperature and humidity profiling using spectral infrared and microwave observations. Part II: Actual retrieval performance in clear-sky and cloudy conditions. *J. Appl. Meteor. Climatol.*, **54**, 2305–2319, doi:10.1175/JAMC-D-15-0005.1.

——, K. T. Halbert, T. A. Supinie, P. M. Marsh, R. L. Thompson, and J. A. Hart, 2017: SHARPpy: An open-source sounding analysis toolkit for the atmospheric sciences. *Bull. Amer. Meteor. Soc.*, **98**, 1625–1636, doi:10.1175/BAMS-D-15-00309.1.

Bonin, T. A., W. G. Blumberg, P. M. Klein, and P. B. Chilson, 2015: Thermodynamic and turbulence characteristics of the southern Great Plains nocturnal boundary layer under differing turbulent regimes. *Bound.-Layer Meteor.*, **157**, 401–420, doi:10.1007/s10546-015-0072-2.

Carlson, T. N., 1998: *Mid-Latitude Weather Systems.* Amer. Meteor. Soc., 507 pp.

Chan, P., and K. Hon, 2011: Application of ground-based, multichannel microwave radiometer in the nowcasting of intense convective weather through instability indices of the atmosphere. *Meteor. Z.*, **20**, 431–440, doi:10.1127/0941-2948/2011/0276.

Cimini, D., M. Nelson, J. Güldner, and R. Ware, 2015: Forecast indices from a ground-based microwave radiometer for operational meteorology. *Atmos. Meas. Tech.*, **8**, 315–333, doi:10.5194/amt-8-315-2015.

Clough, S. A., M. J. Iacono, and J.-L. Moncet, 1992: Line-by-line calculations of atmospheric fluxes and cooling rates: Application to water vapor. *J. Geophys. Res.*, **97**, 15761–15785, doi:10.1029/92JD01419.

Di Natale, G., L. Palchetti, G. Bianchini, and M. Del Guasta, 2017: Simultaneous retrieval of water vapour, temperature and cirrus clouds properties from measurements of far infrared spectral radiance over the Antarctic Plateau. *Atmos. Meas. Tech.*, **10**, 825–837, doi:10.5194/amt-10-825-2017.

Doswell, C. A., and E. N. Rasmussen, 1994: The effect of neglecting the virtual temperature correction on CAPE calculations. *Wea. Forecasting*, **9**, 625–629, doi:10.1175/1520-0434(1994)009<0625:TEONTV>2.0.CO;2.

Ebell, K., E. Orlandi, A. Hünerbein, U. Löhnert, and S. Crewell, 2013: Combining ground-based with satellite-based measurements in the atmospheric state retrieval: Assessment of the information content. *J. Geophys. Res. Atmos.*, **118**, 6940–6956, doi:10.1002/jgrd.50548.

Ermold, B., and V. Morris, 1996: Ceilometer (CEIL): Cloud-base heights (updated hourly). ARM Climate Research Facility Data Archive. Subset used: 13 May–15 June 2002, accessed 13 March 2016, doi:10.5439/1181954.

——, and J. Kyrouac, 1999: Temperature, humidity, winds and pressure system (THWAPS): Meteorological data (updated hourly). ARM Climate Research Facility Data Archive. Subset used: 13 May–25 June 2002, accessed 13 March 2016, doi:10.5439/1025304.

Feltz, W. F., and J. R. Mecikalski, 2002: Monitoring high-temporal-resolution convective stability indices using the ground-based Atmospheric Emitted Radiance Interferometer (AERI) during the 3 May 1999 Oklahoma–Kansas tornado outbreak. *Wea. Forecasting*, **17**, 445–455, doi:10.1175/1520-0434(2002)017<0445:MHTRCS>2.0.CO;2.

——, W. L. Smith, R. O. Knuteson, H. E. Revercomb, H. M. Woolf, and H. B. Howell, 1998: Meteorological applications of temperature and water vapor retrievals from the ground-based Atmospheric Emitted Radiance Interferometer (AERI). *J. Appl. Meteor.*, **37**, 857–875, doi:10.1175/1520-0450(1998)037<0857:MAOTAW>2.0.CO;2.

——, ——, H. B. Howell, R. O. Knuteson, H. Woolf, and H. E. Revercomb, 2003: Near-continuous profiling of temperature, moisture, and atmospheric stability using the Atmospheric Emitted Radiance Interferometer (AERI). *J. Appl. Meteor.*, **42**, 584–597, doi:10.1175/1520-0450(2003)042<0584:NPOTMA>2.0.CO;2.

Gartzke, J., R. Knuetson, G. Przybyl, S. Ackerman, and H. Revercomb, 2017: Comparison of satellite-, model-, and radiosonde-derived convective available potential energy (CAPE) in the Southern Great Plains region. *J. Appl. Meteor. Climatol.*, **56**, 1499–1513, doi:10.1175/JAMC-D-16-0267.1.

Hackel, D., A. Koontz, B. Ermold, K. Gaustad, R. Garcia, and J. Gero, 1994: Atmospheric Emitted Radiance Interferometer (AERI): Channel 1 data (updated hourly). ARM Climate Research Facility Data Archive. Subset used: 13 May–15 June 2002, accessed 13 March 2016, doi:10.5439/1025143.

Ho, S., W. Smith, and H. Huang, 2002: Retrieval of atmospheric temperature and water-vapor profiles by use of combined satellite and ground-based infrared spectral-radiance measurements. *Appl. Opt.*, **41**, 4057–4069, doi:10.1364/AO.41.004057.

Holdridge, D. J., M. Ritsche, J. Prell, and R. Coulter, 2011: Balloon-borne sounding system handbook. ARM Climate Research Facility Rep. ARM TR-029, 28 pp., https://www.arm.gov/publications/tech_reports/handbooks/sonde_handbook.pdf.

Knuteson, R. O., and Coauthors, 2004a: Atmospheric Emitted Radiance Interferometer. Part I: Instrument design. *J. Atmos. Oceanic Technol.*, **21**, 1763–1776, doi:10.1175/JTECH-1662.1.

——, and Coauthors, 2004b: Atmospheric Emitted Radiance Interferometer. Part II: Instrument performance. *J. Atmos. Oceanic Technol.*, **21**, 1777–1789, doi:10.1175/JTECH-1663.1.

Koch, S. E., R. Ware, H. Jiang, and Y. Xie, 2016: Rapid mesoscale environmental changes accompanying genesis of an unusual tornado. *Wea. Forecasting*, **31**, 763–786, doi:10.1175/WAF-D-15-0105.1.

Kyrouac, J., R. Coulter, and D. Holdridge, 1994: Balloon-borne sounding system (BBSS): Research winds, Vaisala pressure, temperature, and relative humidity (updated hourly). ARM Climate Research Facility Data Archive. Subset used: 13 May–25 June 2002, accessed 13 March 2016, doi:10.5439/1150270.

Löhnert, U., and O. Maier, 2012: Operational profiling of temperature using ground-based microwave radiometry at Payerne: Prospects and challenges. *Atmos. Meas. Tech.*, **5**, 1121–1134, doi:10.5194/amt-5-1121-2012.

——, D. D. Turner, and S. Crewell, 2009: Ground-based temperature and humidity profiling using spectral infrared and microwave observations. Part I: Simulated retrieval performance in clear-sky conditions. *J. Appl. Meteor. Climatol.*, **48**, 1017–1032, doi:10.1175/2008JAMC2060.1.

Madhulatha, A., M. Rajeevan, M. V. Ratnam, J. Bhate, and C. V. Naidu, 2013: Nowcasting severe convective activity over southeast India using ground-based microwave radiometer observations. *J. Geophys. Res. Atmos.*, **118**, 1–13, doi:10.1029/2012JD018174.

Markowski, P., and Y. Richardson, 2011: *Mesoscale Meteorology in Midlatitudes*. Vol. 2., John Wiley and Sons, 407 pp., doi:10.1002/9780470682104.

Moller, A. R., 2001: Severe local storms forecasting. *Severe Convective Storms*, *Meteor. Monogr.*, No. 50, Amer. Meteor. Soc., 433–480.

Pushpa Saroja, R., M. Rajasekhar, G. Papa Rao, M. Rajeevan, and G. Bharathi, 2016: Assessment of forecast indices over Sriharikota using ground-based microwave radiometer. *Remote Sensing of the Atmosphere, Clouds, and Precipitation VI*, E. Im, R. Kumar, and S. Yang, Eds., Society of Photo-Optical Instrumentation Engineers (SPIE Proceedings, Vol. 9876), 987633, doi:10.1117/12.2224405.

Rodgers, C. D., 2000: *Inverse Methods for Atmospheric Sounding: Theory and Practice.* Series on Atmospheric, Oceanic and Planetary Physics, Vol. 2, World Scientific, 238 pp.

Serio, C., and Coauthors, 2008: Interferometer for ground-based observations of emitted spectral radiance from the troposphere: Evaluation and retrieval performance. *Appl. Opt.*, **47**, 3909–3919, doi:10.1364/AO.47.003909.

Sisterson, D. L., R. A. Peppler, T. S. Cress, P. J. Lamb, and D. D. Turner, 2016: The ARM Southern Great Plains (SGP) site. *The Atmospheric Radiation Measurement (ARM) Program: The First 20 Years*, *Meteor. Monogr.*, No. 57, Amer. Meteor. Soc., doi:10.1175/AMSMONOGRAPHS-D-16-0004.1.

Smith, W. L., W. F. Feltz, R. O. Knuteson, H. E. Revercomb, H. M. Woolf, and H. B. Howell, 1999: The retrieval of planetary boundary layer structure using ground-based infrared spectral radiance observations. *J. Atmos. Oceanic Technol.*, **16**, 323–333, doi:10.1175/1520-0426(1999)016<0323:TROPBL>2.0.CO;2.

Stull, R. B., 1988: *An Introduction to Boundary Layer Meteorology.* Springer, 666 pp.

Thompson, R. L., R. Edwards, J. A. Hart, K. L. Elmore, and P. Markowski, 2003: Close proximity soundings within supercell environments obtained from the Rapid Update Cycle. *Wea. Forecasting*, **18**, 1243–1261, doi:10.1175/1520-0434(2003)018<1243:CPSWSE>2.0.CO;2.

Trier, S. B., C. A. Davis, D. A. Ahijevych, and K. W. Manning, 2014a: Use of the parcel buoyancy minimum ($B_{\min}$) to diagnose simulated thermodynamic destabilization. Part I: Methodology and case studies of MCS initiation environments. *Mon. Wea. Rev.*, **142**, 945–966, doi:10.1175/MWR-D-13-00272.1.

——, ——, ——, and ——, 2014b: Use of the parcel buoyancy minimum ($B_{\min}$) to diagnose simulated thermodynamic destabilization. Part II: Composite analysis of mature MCS environments. *Mon. Wea. Rev.*, **142**, 967–990, doi:10.1175/MWR-D-13-00273.1.

——, G. S. Romine, D. A. Ahijevych, R. J. Trapp, R. S. Schumacher, M. C. Coniglio, and D. J. Stensrud, 2015: Mesoscale thermodynamic influences on convection initiation near a surface dryline in a convection-permitting ensemble. *Mon. Wea. Rev.*, **143**, 3726–3753, doi:10.1175/MWR-D-15-0133.1.

Turner, D. D., and U. Löhnert, 2014: Information content and uncertainties in thermodynamic profiles and liquid cloud properties retrieved from the ground-based Atmospheric Emitted Radiance Interferometer (AERI). *J. Appl. Meteor. Climatol.*, **53**, 752–771, doi:10.1175/JAMC-D-13-0126.1.

——, R. O. Knuteson, H. E. Revercomb, C. Lo, and R. G. Dedecker, 2006: Noise reduction of Atmospheric Emitted Radiance Interferometer (AERI) observations using principal component analysis. *J. Atmos. Oceanic Technol.*, **23**, 1223–1238, doi:10.1175/JTECH1906.1.

——, E. J. Mlawer, and H. E. Revercomb, 2016: Water vapor observations in the ARM program. *The Atmospheric Radiation Measurement (ARM) Program: The First 20 Years*, *Meteor. Monogr.*, No. 57, Amer. Meteor. Soc., doi:10.1175/AMSMONOGRAPHS-D-15-0025.1.

Wagener, R., S. Xie, and L. Gregory, 2002: 20 km isobaric Rapid Update Cycle grids (ALLRUC20ISOB) (updated daily). ARM Climate Research Facility Data Archive. Subset used: 13 May–25 June 2002, accessed 13 March 2016, http://www.archive.arm.gov/discovery/#v/results/s/s::ALLRUC20ISOB.

Wagner, T. J., W. F. Feltz, and S. A. Ackerman, 2008: The temporal evolution of convective indices in storm-producing environments. *Wea. Forecasting*, **23**, 786–794, doi:10.1175/2008WAF2007046.1.

Weckwerth, T. M., and Coauthors, 2004: An overview of the International H_2O Project (IHOP_2002) and some preliminary highlights. *Bull. Amer. Meteor. Soc.*, **85**, 253–277, doi:10.1175/BAMS-85-2-253.

——, K. J. Weber, D. D. Turner, and S. M. Spuler, 2016: Validation of a water vapor micropulse differential absorption lidar (DIAL). *J. Atmos. Oceanic Technol.*, **33**, 2353–2372, doi:10.1175/JTECH-D-16-0119.1.